Received: 22 September 2016 | Revised: 17 March 2017 | Accepted: 4 April 2017

DOI: 10.1002/nbm.3742

WILEY NMR IN BIOMEDICINE

RESEARCH ARTICLE

Simultaneous use of linear and nonlinear gradients for B_1^+ inhomogeneity correction

Koray Ertan[1,2] | Ergin Atalar[1,2]

[1] National Magnetic Resonance Research Center (UMRAM), Bilkent University, Bilkent, Ankara, Turkey

[2] Department of Electrical and Electronics Engineering, Bilkent University, Bilkent, Ankara, Turkey

Correspondence
Ergin Atalar, National Magnetic Resonance Research Center (UMRAM), Bilkent University, Bilkent, Ankara, Turkey.
Email: ergin@ee.bilkent.edu.tr

Funding information
TUBITAK (The Scientific and Technological Research Council of Turkey), Grant/Award Number: 1001-112E555

The simultaneous use of linear spatial encoding magnetic fields (L-SEMs) and nonlinear spatial encoding magnetic fields (N-SEMs) in B_1^+ inhomogeneity problems is formulated and demonstrated with both simulations and experiments. Independent excitation *k*-space variables for N-SEMs are formulated for the simultaneous use of L-SEMs and N-SEMs by assuming a small tip angle. The formulation shows that, when N-SEMs are considered as an independent excitation *k*-space variable, numerous different *k*-space trajectories and frequency weightings differing in dimension, length, and energy can be designed for a given target transverse magnetization distribution. The advantage of simultaneous use of L-SEMs and N-SEMs is demonstrated by B_1^+ inhomogeneity correction with spoke excitation. To fully utilize the independent *k*-space formulations, global optimizations are performed for 1D, 2D RF power limited, and 2D RF power unlimited simulations and experiments. Three different cases are compared: L-SEMs alone, N-SEMs alone, and both used simultaneously. In all cases, the simultaneous use of L-SEMs and N-SEMs leads to a decreased standard deviation in the ROI compared with using only L-SEMs or N-SEMs. The simultaneous use of L-SEMs and N-SEMs results in better B_1^+ inhomogeneity correction than using only L-SEMs or N-SEMs due to the increased number of degrees of freedom.

KEYWORDS

B_1^+ inhomogeneity, excitation *k*-space, nonlinear gradients, simultaneous use of linear and nonlinear gradients, small tip angle, spoke excitation

1 | INTRODUCTION

In MRI, spatially selective excitation aims to excite the desired transverse magnetization distribution. For this purpose, the design of the RF pulse and gradients requires an inverse solution to the Bloch equation, which is still an open problem. In Reference [1], the small tip angle approximation overcomes this problem by introducing the excitation *k*-space concept. In a reasonable design with linear spatial encoding magnetic fields (L-SEMs), a *k*-space trajectory should cover significant energy in the Fourier transform of the target transverse magnetization distribution. Furthermore, high main field strengths (>1.5 T) have become desirable due to their high SNR,[2] but B_1^+ inhomogeneity can degrade the image quality significantly.[2,3] RF shimming[4] and parallel transmission[5,6] were proposed to mitigate B_1^+ inhomogeneity. Another method is to use a three-dimensional RF pulse. In the excitation *k*-space framework, mitigation of B_1^+ inhomogeneity leads to a 3D target excitation pattern, which can be excited with a 3D excitation *k*-space approach. In a multi-dimensional target transverse magnetization scenario, energy in the excitation *k*-space spreads to multiple dimensions. Therefore, a reasonable excitation trajectory should cover most of the energy in the excitation *k*-space and should be dense enough to avoid aliasing, which results in an impractical RF pulse with very long durations. However, because the Fourier transform of the target transverse magnetization is unique, the selection and design of a reasonable *k*-space trajectory have only limited flexibility. In the literature, spoke excitation is generally used for slice selective B_1^+ inhomogeneity with either fixed spoke locations[7] or optimized spoke locations.[8,9] Although various trajectory choices exist, these trajectories are similar in terms of length, dimension and frequency weightings, which limits the degrees of freedom in the RF

Abbreviations used: B_1^+, RF frequency left-handed polarized magnetic field for excitation of spins; L-SEM, linear spatial encoding magnetic field; N-SEM, nonlinear spatial encoding magnetic field; PNS, peripheral nerve stimulation; RMSE, root mean square error; VOI, volume of interest

pulse optimization. Possible solutions for increasing the degrees of freedom in the multi-dimensional RF pulse design problem should be investigated. Additional degrees of freedom can lead to more homogeneous excitation profiles and shorter RF pulse durations for more off-resonance robustness and shorter echo times.

One way of obtaining additional degrees of freedom is by using nonlinear spatial encoding magnetic fields (N-SEMs) and L-SEMs in RF pulse design problems. The Fourier transform relationship between the excitation *k*-space and transverse magnetization distribution is broken with the addition of an independent N-SEM channel, since N-SEMs and L-SEMs are coupled via spatial variables. Some studies that include the phase accumulation due to N-SEM channels in the RF pulse design problem already exist.[10,11] Some other studies explicitly define the excitation *k*-space variables for N-SEMs, which satisfies the Fourier transform relationship between the excitation *k*-space and transverse magnetization distribution under special conditions.[12,13] In our study, the independent excitation *k*-space dimension for each N-SEM is defined when they are simultaneously used with L-SEMs. Furthermore, the Fourier transform relation between the excitation *k*-space in higher dimensions (>3) and transverse magnetization distribution is re-established with the formulations in the general case of the simultaneous use of L-SEMs and N-SEMs. It is also shown that an increase in the dimension of the excitation *k*-space can lead to an infinite number of different trajectories.

This study provides an excitation *k*-space formulation for the simultaneous use of L-SEMs and N-SEMs in the RF excitation problem. The proposed formulation demonstrates the increase in the number of degrees of freedom with higher-dimensional Fourier transform. An increase in the number of degrees of freedom is demonstrated for a slice selective B_1^+ inhomogeneity correction problem using three spoke locations. Comparisons of the use of only L-SEMs, the use of only N-SEMs and their simultaneous use are presented for slice selective one- and two-dimensional (RF power unlimited and limited) simulations, as well as for slice selective 2D experiments.

2 | THEORY

In Reference [1], an analytical expression for the excitation profile for a given RF and gradient waveforms is provided as follows:

$$M_{xy}(\boldsymbol{r}) = \mathrm{i}\gamma M_0 \int_0^T B_1(t) e^{-i\gamma \boldsymbol{r}\cdot\int_t^T \boldsymbol{G}(s)ds} dt. \tag{1}$$

Here, definitions of various variables are adapted to be consistent with N-SEMs. $\boldsymbol{r} = [x/x_{\mathrm{VOI}}\ \ y/y_{\mathrm{VOI}}\ \ z/z_{\mathrm{VOI}}]$ is a unitless vector of the normalized spatial coordinates, which are the physical spatial coordinates divided by the length (x_{VOI}, y_{VOI}, z_{VOI}) of the volume of interest (VOI) in the respective dimensions. $\boldsymbol{G}(s) = [\ G_x(s)x_{\mathrm{VOI}}\ \ G_y(s)y_{\mathrm{VOI}}\ \ G_z(s)z_{\mathrm{VOI}}]$ is a vector of gradient temporal dependencies multiplied by the VOI in the respective dimension. M_0 is the initial longitudinal magnetization, γ is the gyromagnetic ratio, $B_1(t)$ is the time envelope of the transmit signal and T is the duration of the RF pulse. Although Equation 1 assumes that B_1^+ is spatially homogeneous, the spatial dependency of B_1^+ will later be included by assuming spatiotemporal separability. Further algebraic steps in Reference [1] establish a Fourier transform relationship between the RF pulse and excitation profile:

$$\begin{aligned} M_{xy}(\boldsymbol{r}) &= \mathrm{i}\gamma M_0 \int_K W(\boldsymbol{k}) S(\boldsymbol{k}) \mathrm{e}^{\mathrm{i}2\pi \mathrm{r}\cdot\boldsymbol{k}} \mathrm{d}\boldsymbol{k} \\ \boldsymbol{S}(\boldsymbol{k}) &= \int_0^T \delta(\boldsymbol{k}(t)-\boldsymbol{k}) |\dot{\boldsymbol{k}}(t)| \mathrm{d}t \\ \boldsymbol{k}(t) &= -\frac{\gamma}{2\pi}\int_t^T \boldsymbol{G}(s)\mathrm{d}s \\ W(\boldsymbol{k}(t)) &= 2\pi B_1(t)/|\gamma \boldsymbol{G}(t)| \end{aligned} \tag{2}$$

where $W(\boldsymbol{k}(t))$ is the spatial frequency weighting function and $S(\boldsymbol{k})$ is the sampling function. The excitation *k*-space concept is introduced for only L-SEMs by assuming that the *k*-space trajectory does not cross itself. The *k*-space variables are also unitless because normalized spatial coordinates are used in this study.

N-SEMs can be included in the above equations with a slight manipulation of the derivation. To simplify the equations for better visualization, only one additional N-SEM is considered in the formulation; however, generalization to multiple N-SEMs is trivial. Under the assumption of spatiotemporal separability, the $\hat{z}$-component of the magnetic field produced by the nonlinear gradient coil can be written as $u(r)G_u(t)$. To be consistent with the L-SEMs, $u(r)$ is also a unitless, normalized spatial dependency of the N-SEM, such that the difference between the maximum and minimum values is unity within the field of view. $G_u(t)$ is the temporal dependency of the magnetic field strength. Addition of the N-SEM together with the small tip angle approximation results in

$$M_{xy}(r) = \mathrm{i}\gamma M_0 \int_0^T B_1(t) e^{-i\gamma\left(r\cdot\int_t^T G(s)ds + u(r)\int_t^T G_u(s)ds\right)} dt. \tag{3}$$

Here, because $u(r)$ is a function of the other spatial variables, a completely independent *k*-space variable for N-SEM cannot be introduced. Inserting a delta function into Equation 3 and introducing an independent dummy space variable, u, leads to

$$M_{xy}(r) = i\gamma M_0 \int_{-\infty}^{+\infty} \int_0^T \delta\ (u(r)-u) B_1(t) e^{-i\gamma\left(\tilde{r}\cdot\int_t^T \tilde{G}(s)ds\right)} dt du. \tag{4}$$

In Equation 4, $\tilde{r} = [x/x_{ROI}\ \ y/y_{ROI}\ \ z/z_{ROI}\ u]$ is a vector of regular normalized Cartesian coordinates concatenated with the dummy space variable u. $\tilde{G}(s) = [\ G_x(s)x_{ROI}\ \ G_y(s)y_{ROI}\ \ G_z(s)z_{ROI}\ G_u(s)]$ is the vector of temporal dependencies for both L-SEMs and the N-SEM. Application of the same algebraic procedure in the derivation of Equation 2 from Equation 1 yields

$$\begin{aligned} M_{xy}(r) &= i\gamma M_0 \int_{-\infty}^{+\infty} \delta(u(r)-u) \int_K W\left(\tilde{k}\right) S\left(\tilde{k}\right) e^{i2\pi \tilde{r}\cdot\tilde{k}} d\tilde{k}\, du \\ S\left(\tilde{k}\right) &= \int_0^T \delta\left(\tilde{k}(t)-\tilde{k}\right) |\tilde{k}(t)| dt \\ \tilde{k}(t) &= -\frac{\gamma}{2\pi}\int_t^T \tilde{G}(s) ds \\ W\left(\tilde{k}(t)\right) &= 2\pi B_1(t)/|\gamma \tilde{G}(t)|. \end{aligned} \tag{5}$$

In Equation 5, the addition of an N-SEM channel increases the dimension of the excitation k-space to four, while the conventional excitation k-space is 3D in Equation 2. Equation 5 further suggests that the k-space variable corresponding to the N-SEM channel can be treated as an independent k-space variable. Therefore, design can be performed for the four-dimensional spatial frequency weighting function, $W(\tilde{k})$, sampled at the 4D trajectory, $S(\tilde{k})$.

Equation 5 can be utilized in two different ways. First, if the RF and gradient waveforms are known, the 4D excitation k-space can be constructed. Clearly, a 4D inverse Fourier transform of the excitation k-space is a function of the three conventional spatial variables x, y, z and the additional dummy space variable u. In this case, the resulting transverse magnetization will be the 4D inverse Fourier transform of the excitation k-space, calculated only at the points lying on $\delta(u(r) - u)$, which is an expression of the 3D object in a 4D space.

The second and more beneficial approach would be to design an excitation k-space for a desired transverse magnetization distribution. In a 4D space, a 3D target excitation distribution can be mapped onto $\delta(u(r) - u)$. Afterwards, the 4D space can be filled freely at all points except those on $\delta(u(r) - u)$ since only the values on the object, $\delta(u(r) - u)$, determine the actual excitation profile. Depending on how the 4D space is filled, its Fourier transform, which determines the multiplication of $W\left(\tilde{k}\right)$ and $S\left(\tilde{k}\right)$, can be manipulated to better fit the design criteria. Therefore, the ability to change the Fourier transform of the 4D space can lead to infinitely many different k-space trajectories and spatial frequency weighting functions with the same excitation profile. Smart design of the 4D space might fulfill different excitation criteria, such as short k-space trajectories or low RF power excitation pulses.

To explain the freedom, a target excitation problem is considered in 1D. Figure 1A shows the target excitation profile for a line object. One linear gradient (x-SEM) and one nonlinear gradient (x^2-SEM) are considered to excite the target excitation profile on the line object. Notably, although the x^2-gradient is not suitable for the Maxwell equations in the 3D volume, it is physically realizable on the $y = z = 0$ line. In Figure 1B, the target excitation profile is mapped onto a parabola defined by $\delta(u - x^2)$. For the design goals, only the values on the parabola in the u-x plane are specified, and the values on the rest of the plane can be chosen freely without altering the target excitation. In Figure 2A, the u-x plane is constructed using this freedom such that it does not have any variation in the nonlinear axes. The corresponding excitation k-space in Figure 2F contains samples only on the k_x-axis, which demonstrates the use of only L-SEM. Alternatively, the u-x plane in Figure 2B does not have any variation in the linear direction, which results in 1D excitation k-space samples only on the k_u-axis (Figure 2G) while using only the N-SEM. In Figure 2C,H, the u-x plane is constructed such that it does not vary in the direction of a specific axis. Therefore, the Fourier transform is again squeezed into one dimension, which allows the use of a 1D k-space trajectory and requires the use of both x- and x^2-SEMs. In Figure 2D, all of the unspecified regions are set to 0, resulting in a Fourier transform in Figure 2I that requires a longer trajectory but has lower frequency weightings. Similarly, Figure 2E,J shows an example design that is suitable for a concentric ring-shaped trajectory. Thus, Figure 2 demonstrates that the Fourier transform of the

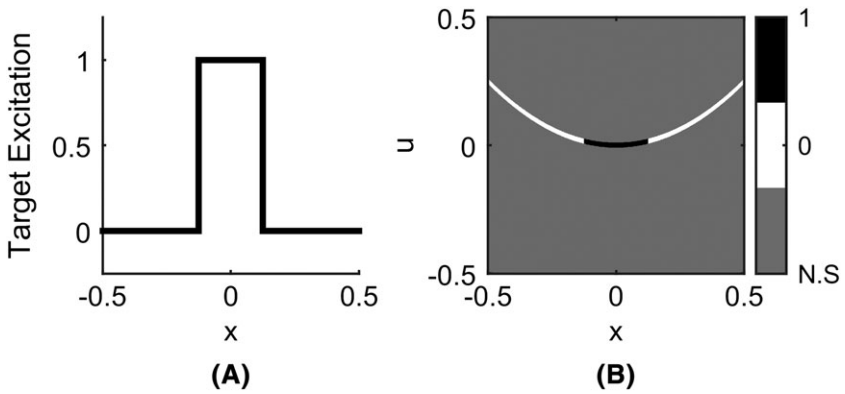

FIGURE 1 An example target excitation demonstrating a regular slice selection with simultaneous use of x and x^2 gradients. A, 1D normalized target excitation profile. B, Target excitation profile mapped onto $\delta(u - x^2)$. Gray regions in the u-x plane are not constrained by the excitation profile. N.S. stands for "not specified"

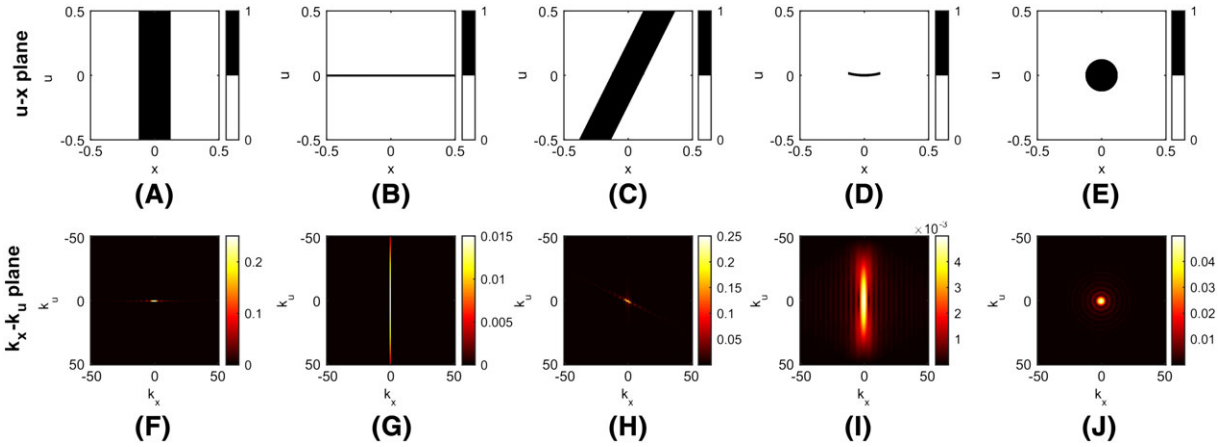

FIGURE 2 *u-x* plane approach to demonstrate that many different excitation *k*-spaces (second row) can be used to excite the same transverse magnetization distribution as in Figure 1A. A-E, The gray region in Figure 1B is filled freely with different distributions that vary as a function of only a linear variable A, only a nonlinear variable B, or a specific combination of linear and nonlinear variables C. The entire gray region in Figure 1B is set to 0 D, and only the circular region at the center is set to 1 E. F-J, Fourier transformations of the constructed *u-x* plane distributions to demonstrate the excitation *k*-spaces in the increased dimension

target transverse magnetization can be altered by filling the unrestricted regions in the *u-x* plane. This freedom can lead to various excitation *k*-space trajectories that differ in dimensionality, energy or length, but lead to exactly the same excitation profile in space.

To extend the previous example to a multi-dimensional excitation problem, B_1^+ inhomogeneity correction as well as slice selection are investigated using L-SEMs and an N-SEM together. Spoke excitation is a suitable choice for such a design purpose. In the conventional spoke excitation, the best spoke locations can be optimized in a 2D excitation *k*-space to correct the 2D B_1^+ inhomogeneity. In contrast, spoke excitation with the simultaneous use of L-SEMs and an N-SEM provides a 3D excitation *k*-space to correct 2D B_1^+ inhomogeneity, which increases the degrees of freedom in the design problem. Assuming a small tip angle and spatiotemporally separability of the B_1^+ field, the optimization problem can be written as

$$\min\left(\iint_{\mathrm{ROI}}\left|1-\left|b_1(x,y)\sum_{n=1}^{N}a_n e^{i2\pi(k_{xn}x+k_{yn}y+k_{un}u(x,y))}e^{-i\gamma(N-n)\Delta B_0(x,y)\Delta T}\right|\right|^2 dx\,dy\right)$$
$$b_1(x,y)=B_1(x,y)/\iint_{\mathrm{ROI}}|B_1(x,y)|dx\,dy \tag{6}$$

where $b_1(x, y)$ is the normalized B_1^+ distribution in the slice, a_n is the normalized amplitude of the *n*th spoke, ΔB_0 is the B_0 inhomogeneity term, ΔT is the time between the consecutive RF pulses, $u(x, y)$ is the magnetic field profile of the nonlinear channel, and k_{xn}, k_{yn}, and k_{un} are the *k*-space location coordinates for the *n*th spoke. Even if the field profile of the nonlinear gradient coil is a 3D function, it can be considered as a 2D function by assuming thin slice selection with the spoke excitation.

Although SAR is not considered in the optimizations except for a set of 2D simulations, a parameter *P* is defined as the sum-of-squares normalized spoke amplitude to evaluate the SAR performance. Because SAR is proportional to the time integral of the squared RF pulse amplitude and identical RF pulse waveforms are used for all spokes independent of the spoke number, *P* is also proportional to the SAR.

$$P=\sum_{1}^{N}|a_n|^2. \tag{7}$$

No flip angle compensation corresponds to one spoke with amplitude 1 ($a_1 = 1$). This is called the uncorrected case and leads to a *P* value of 1. When multiple spokes are used to correct the excitation profile, *P* also indicates the ratio of the SAR for uncorrected and corrected sequences for the same average flip angle. Because RF pulse waveforms and durations are considered to be identical for all spokes independent of the spoke number, the *P* parameter does not consider the tradeoff that SAR would decrease if an RF pulse for the one-spoke excitation was allowed to have the same duration in multiple-spoke excitations. In RF power-limited 2D simulations, *P* is bounded by 1, which ensures that RF power does not increase for the corrected excitation profile with respect to the uncorrected excitation.

3 | METHODS

To demonstrate the advantage of using an additional N-SEM for B_1^+ inhomogeneity correction, three cases are compared: L-SEMs alone, the N-SEM alone and both sets of fields simultaneously. This comparison is performed using 1D and 2D simulations as well as an experimental study on a phantom.

3.1 | Optimizations

Optimizations use the structure in Equation 6. In all of the optimization problems, the number of spokes, N, is chosen as 3 to limit the duration of the excitation pulse. Because inhomogeneity correction is only performed for the amplitude of the excitation, relative positions of the spokes are not important, and therefore one spoke location can be chosen arbitrarily. In our design, the first spoke is placed at the origin. Two spoke locations and the complex weightings of the three RF pulses are optimized. The B_0 inhomogeneity is ignored in the simulations but considered in the experiments. As a performance measure for each case, a reduction in the flip angle inhomogeneity is defined as $(1-\sigma_{corrected}/\sigma_{uncorrected})$, where $\sigma_{uncorrected}$ and $\sigma_{corrected}$ indicate the standard deviations of the normalized flip angle map for uncorrected and corrected cases, respectively.

In 1D simulations, a B_1^+ inhomogeneity profile is generated as a quadratic function of x, as in Figure 5F later, to demonstrate the advantage of simultaneous use of L-SEM and N-SEM. The only available gradients are x and $u(\boldsymbol{r}) = x^2$ gradients. Therefore, while using only the L-SEM, the spoke locations are optimized only on the k_x line. Similarly, while using only the N-SEM, spoke locations are optimized on the k_u line; however, while simultaneously using L-SEM and N-SEM, spoke locations are optimized in a plane defined by the k_x and k_u lines.

For 2D simulations, the N-SEM dependency is assumed to be $x^2 + y^2$. For only L-SEM, spoke locations are determined in the plane defined by k_x and k_y. For only N-SEM, spoke locations are on the k_u line. For simultaneous use, spokes are placed on a 3D volume defined by k_x, k_y, and k_u. For RF power-constrained simulations, P values are limited to 1, which corresponds to the same RF power as for one-spoke excitation. In the experiments, free optimization parameters are the same as those in 2D simulations except that B_0 inhomogeneity is also accounted for.

Optimizations are performed in MATLAB 2014b (MathWorks, Natick, MA, USA). The built-in MATLAB function "GlobalSearch" has been used. The algorithm uses the "Scatter Search Algorithm" to select multiple starting points at different basins of attraction from the given initial value. A predefined local solver operates on each starting point to find the global optimum. Further details of the algorithm are explained in Reference [14]. Another built-in function, "fmincon," is used with the "interior point algorithm" as a local solver. In the optimizations, an initial point that is chosen as zero is used as an initial guess for the first local solver call. The performance of the method is sensitive to the initial guess; however, the generation of many trial points decreases its effect. In the simulations, the amplitude of each RF pulse is limited to 5, and normalized k-space locations are bounded between −10 and 10. The maximum number of trial points is defined as 1000, which is also the stopping criterion. In the experiments, the maximum duration of the optimization is limited to 100 s as an additional stopping criterion.

3.2 | Experiments

Experiments are conducted using a 3 T scanner (Magnetom Trio A Tim, Siemens) with a Siemens phantom. For the experiments, a custom-made nonlinear gradient coil is manufactured. Although the nonlinear gradient coil has three independent channels as in Figure 3A, only one channel with 60 turns is used, since the aim of the paper is to demonstrate the increase in the number of degrees of freedom even with the addition of one N-SEM. However, extension to multiple channels can be trivially considered by increasing the computational cost of the optimization. The nonlinear gradient coil is wound on a plastic cylinder with a diameter of 20 cm, and the wire diameter is 2.1 mm. The loops are in the circumferential direction, which cancels the net torque. The phantom is placed next to the coil, as in Figure 3A. The nonlinear gradient coil is driven with an external gradient amplifier (GA-300 amplifier, Performance Controls, Montgomeryville, PA, USA), which is controlled by a signal generator. The feed cables for the gradient coil are connected to the Faraday cage with a 10 nF filter capacitor to shield the RF noise. Inside the scanner bore, feed cables are kept parallel to B_0; therefore, there is no force experienced by the feed cables, and the current on these wires does not contribute to the magnetic field in the z-direction.

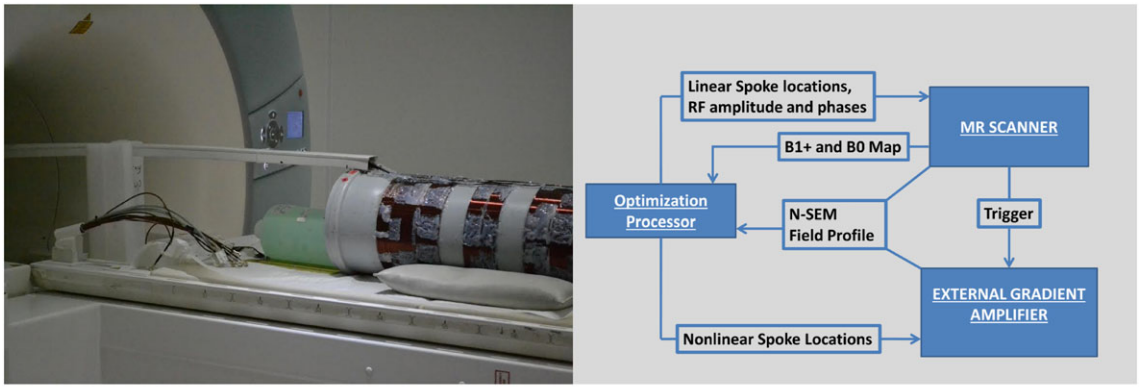

FIGURE 3 Experimental setup and procedure. A, Placement of the Siemens phantom and the nonlinear gradient coil. The nonlinear gradient coil has three independent channels with 60, 30, and 60 turns; however, only the closest channel to the phantom is used. B, Schematic diagram for the experimental procedure. Before the optimization, B_0 and B_1 maps and the spatial dependency of the N-SEM are acquired. After optimization is performed, the linear spoke and RF parameters are sent to the MR scanner and the nonlinear spoke locations are sent to the external gradient amplifier

Considering the experimental procedure in Figure 3B, some pre-scans are required at the beginning of the experiment. First, a B_0 map is acquired using the phase difference between two GRE images with different echo times. A custom-built RF transmit and receive coil with rectangular shape is tuned and matched with distributed capacitors. The B_1^+ map of the RF coil is acquired with a Bloch-Siegert-shift based sequence.[15] The magnetic field profile of the nonlinear gradient coil is measured from the phase difference between a reference GRE image and another GRE image with the same echo time and a small blip of current applied to the nonlinear gradient coil during the phase encoding. Alternatively, if the object location relative to the coil is known, the spatial dependency of the magnetic field produced by the nonlinear gradient coil can be calculated using the Biot-Savart law. After obtaining the required B_0, B_1, and gradient coil field maps, the RF and spoke parameters are optimized. The amplitudes and phases of the RF pulses, together with the linear gradient moments for spoke locations, are used by the scanner. The control circuit of the external gradient amplifiers is programmed according to the required nonlinear gradient waveform, which is determined by the k_u component of the spoke locations.

For the comparison of the three different cases, the corresponding pulse sequences in Figure 4 are used. Between the RF pulses, *x*, *z*, and *u* gradients are used to realize the required spoke locations. As in previous work,[16] the slice selection gradients are always positive during the RF pulse, orienting the spokes in the same direction and making the excitation robust to B_0 inhomogeneity and eddy current effects during the RF pulses. The duration of each RF pulse is 1.5 ms, and the time between the RF peaks is 2.94 ms. All input maps and resulting sequence maps are acquired with 128 × 128 resolution in a 2.5 mm thick coronal slice with a FOV of 25 cm for both dimensions. Flip angle maps are obtained by using the double-angle method with average flip angles of 35° and 70° and a T_R of 2.5 s (Figure 9D-F later).

4 | RESULTS

The results of this study are presented in subcategories: 1D simulations, 2D simulations, and experimental results. Detailed information about the standard deviation of the resulting excitation profiles, *P*, *k*-space locations, and RF parameters are provided in Table 1 for all of the simulations and the experiment.

4.1 | 1D simulations

In Figure 5F, the yellow plot shows an example B_1 inhomogeneity profile in 1D. An ideal excitation profile with perfect homogeneity is shown with the dashed line. After optimization for three different cases, corrected excitation profiles are also provided in Figure 5F. As previously explained, the *u*-*x* plane approach can provide another interpretation of the results. The target excitation profile, which is the inverse of the B_1 profile, is mapped onto $\delta(u - x^2)$ in Figure 5A. All other values except the parabola in the *u*-*x* plane are not constrained by the actual problem. However, using only L-SEMs or the N-SEM leads to spoke locations only at the k_x line or the k_u line, respectively, as shown in Figure 5E. This situation causes 1D variations in the *u*-*x* plane for the respective cases in Figure 5B,C, which is possibly suboptimal. In contrast, the simultaneous use of L-SEM and N-SEM allows arbitrary variation in the entire *u*-*x* plane, as in Figure 5D. Another approach using the same degrees of freedom is shown in Figure 5E, where spoke locations for the simultaneous L-SEM/N-SEM excitation can be placed over the entire 2D k_x-k_u plane.

In the 1D simulations, the standard deviations of the excitation profile from unity are 0.14, 0.021, 0.128, and 0.005 for uncorrected, corrected with only L-SEMs, only N-SEM, and simultaneous use, respectively. Using only L-SEMs provides an 85% reduction in the flip angle inhomogeneity. Because optimization with only L-SEMs results in a higher spoke location, a high-frequency oscillatory excitation profile is observed in Figure 5F. The use of only N-SEM yields poor performance with an insignificant (7%) reduction in the inhomogeneity. The reason for such a poor

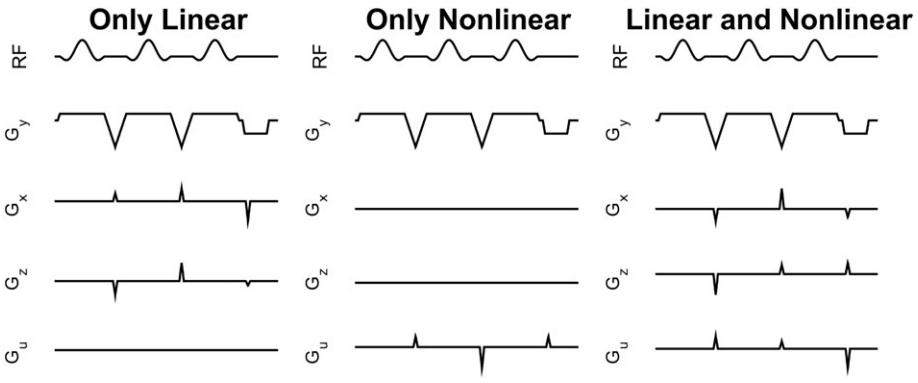

FIGURE 4 Sequence diagrams for three cases. Each has three apodized sinc pulses (three spokes) with slice selection in the *y*-direction. Slice selection is always performed with a positive gradient (flyback trajectory). Between the RF pulses, other linear and nonlinear gradients are used for the multi-dimensional excitation trajectory. For all cases, the phase and amplitude of the RF pulses as well as gradient blips are optimized. The proposed technique in this study is the simultaneous use of linear and nonlinear gradients (third row)

TABLE 1 Results from the simulations and experiments. The standard deviation (σ), P, optimized RF parameters, and k-space locations for all spokes are provided. S1, S2, and S3 represent the first, second, and third spokes, respectively

		Only linear			Only nonlinear			Linear + nonlinear		
1D	σ	0.021			σ	0.128		σ	0.005	
	P	1.03			P	0.95		P	2.34	
		S1	S2	S3		S1	S2	S3	S1	S2	S3
	$\lvert a_n\rvert$	0.13	1	0.11	$\lvert a_n\rvert$	0.94	0.18	0.19	1.02	0.81	0.8
	$\angle a_n$	0	1.79	0.44	$\angle a_n$	0	1.36	1.80	0	2.06	2.78
	k_x	0	−1.62	−4.34	k_x	0	0	0	0	−1.00	−0.49
	k_{x^2}	0	0	0	k_{x^2}	0	4.39	−3.98	0	−0.96	−2.10
2D (RF power unlimited)	σ	0.097			σ	0.329		σ	0.021	
	P	1.09			P	15.17		P	2.53	
		S1	S2	S3		S1	S2	S3	S1	S2	S3
	$\lvert a_n\rvert$	0.55	0.67	0.58	$\lvert a_n\rvert$	2.48	1.06	2.81	1.33	0.13	0.86
	$\angle a_n$	0	1.43	1.35	$\angle a_n$	0	3.43	3.38	0	5.75	4.50
	k_x	0	−0.72	−0.29	k_x	0	0	0	0	−0.16	0.28
	k_y	0	0.33	0.89	k_y	0	0	0	0	0.77	−0.25
	$k_{x^2+y^2}$	0	0	0	$k_{x^2+y^2}$	0	−2.67	−0.18	0	0.29	−0.59
2D (RF power limited)	σ	0.097			σ	0.329		σ	0.035	
	P	1.00			P	1.00		P	1.00	
		S1	S2	S3		S1	S2	S3	S1	S2	S3
	$\lvert a_n\rvert$	0.61	0.60	0.52	$\lvert a_n\rvert$	0.77	0.33	0.55	0.60	0.47	0.64
	$\angle a_n$	0	5.75	4.50	$\angle a_n$	0	1.07	0.00	0	5.15	6.06
	k_x	0	−0.41	−0.75	k_x	0	0	0	0	0.59	0.16
	k_y	0	−0.55	0.32	k_y	0	0	0	0	−0.59	−0.27
	$k_{x^2+y^2}$	0	0	0	$k_{x^2+y^2}$	0	2.07	−1.55	0	−1.36	−0.55
Experiment	$\sigma_{expected}$	0.119			$\sigma_{expected}$	0.142		$\sigma_{expected}$	0.095	
	$\sigma_{measured}$	0.143			$\sigma_{measured}$	0.158		$\sigma_{measured}$	0.120	
	P	1.11			P	1.31		P	1.25	
		S1	S2	S3		S1	S2	S3	S1	S2	S3
	$\lvert a_n\rvert$	0.16	1.02	0.21	$\lvert a_n\rvert$	0.41	0.92	0.54	0.20	0.20	1.08
	$\angle a_n$	0	3.68	2.75	$\angle a_n$	0	2.45	0.40	0	2.70	2.48
	k_x	0	−1.62	−0.13	k_x	0	0	0	0	0.34	−0.78
	k_z	0	−3.54	−0.65	k_z	0	0	0	0	−1.47	−1.63
	k_u	0	0	0	k_u	0	−0.09	−0.43	0	0.06	−0.65

improvement is that the x^2 field profile can only perform symmetrical correction around 0, which does not match with the inverse of the B_1^+ profile. Simultaneous use almost ideally corrects the B_1^+ inhomogeneity, with a 96% reduction in the inhomogeneity.

In this example, using only the N-SEM provides almost no correction. Using only L-SEMs significantly corrects the excitation profile; however, simultaneous use leads to a fourfold lower standard deviation of the excitation profile with almost perfect correction.

4.2 | 2D simulations

2D simulations aim to demonstrate that the advantage of simultaneously using L-SEMs and N-SEM is also valid for a more realistic scenario involving B_1 inhomogeneity correction as well as slice selection. Example B_1 inhomogeneity is assumed as in Figure 6A. Figure 6B-D shows the resulting corrected excitation profiles for only L-SEMs, only the N-SEM, and simultaneous use, respectively. Furthermore, for the same B_1 inhomogeneity, RF power limited simulations have been performed, and the P value is upper bounded by 1, which corresponds to one-spoke or uncorrected excitation. Resulting homogeneity and RF power levels as well as spoke locations are shown in Table 1. Simultaneous use performed better than only L-SEMs and only the N-SEM for both RF power-limited and RF power-unlimited sets. Similarly to the 1D simulation, the use of only the N-SEM provides poor correction of the excitation profile. For both RF power-limited and power-unlimited cases, although the excitation profiles differ slightly, standard deviations inside the ROI are the same if only L-SEMs or only the N-SEM are considered. For simultaneous use, a limitation on the RF power causes a slight increase in the inhomogeneity of the excitation profile. However, the RF power limitation does not affect the homogeneity correction performance significantly while decreasing the RF amplitudes for each case. In 2D simulations, the standard deviation of the B_1^+ inhomogeneity was 45%. For both the RF power-unlimited and RF power-limited sets, the standard deviations are reduced by 78% and 27% for only L-SEMs and only the N-SEM, respectively. For simultaneous use, the standard deviation decreased by 95% and 92% for the RF power-unlimited and RF power-limited cases. Although the RF power-limited and RF power-unlimited cases result in different spoke locations and RF amplitudes, the final standard deviations are almost the same for only L-SEMs or only the N-SEM. This is an indication that there might be multiple optimal solutions for each case. All three cases show that when P is included in the optimization there can still be solutions that provide near-optimal standard deviations. For the RF power-unlimited case, P is increased to 1.1, 15.2, and 2.5 for only L-SEMs, only the N-SEM, and simultaneous use, respectively. When the P values are limited to 1, each case resulted in a P value of 1. Expectedly, the solution of the optimization problem resulted in the highest possible P value since an increase in the RF power can result in decreased inhomogeneity.[17] Alternatively, a P criterion can be inserted into the cost function with an adaptable weighting to provide a tradeoff between RF power and homogeneity.

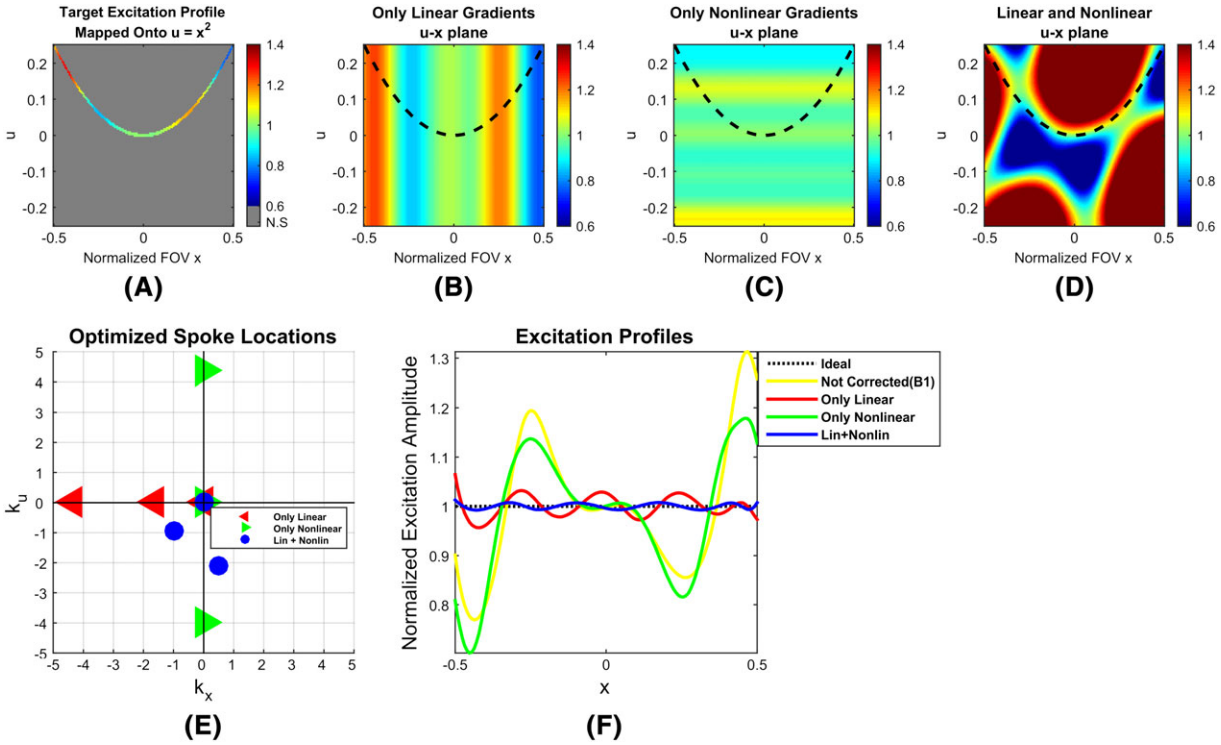

FIGURE 5 1D simulation results. A, 1D target excitation profile is mapped onto $\delta(u - x^2)$. N.S. stands for "not specified." B-D, The resulting distributions in the u-x plane after optimization for only linear, only nonlinear, and simultaneous use of both, respectively. Only the values on the dashed parabolas correspond to actual correction. E, Spoke locations for three different cases, including the central spoke for each case. F, Uncorrected excitation profile due to B_1 inhomogeneity, ideal perfectly homogeneous excitation profile, corrected with only L-SEMs, corrected with only the N-SEM, and corrected with simultaneous use of L-SEMs and the N-SEM

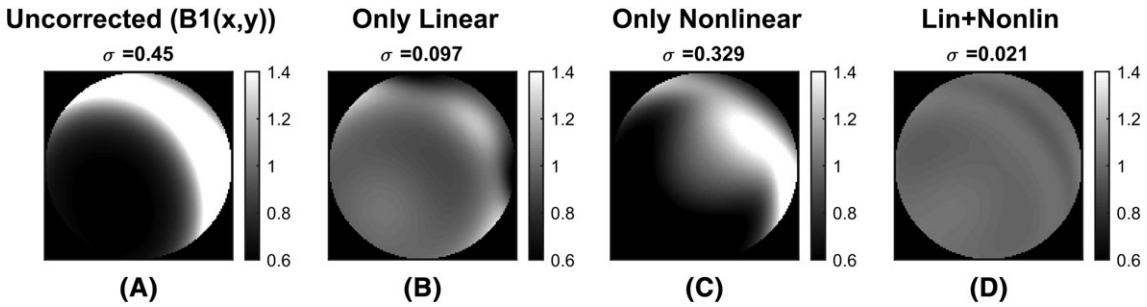

FIGURE 6 2D simulation results. Available gradients are x, y, and $x^2 + y^2$. A, Example B_1 inhomogeneity (uncorrected excitation profile). B-D, Comparison of resulting excitation profiles corrected with only L-SEM, only N-SEM, and simultaneous use of both. RF power-limited solutions are presented in this figure

To give a sense of the required computational power for the optimization problems, the details are provided for 2D RF power-unlimited cases as an example. For each method, generation and analyses of 1000 trial points are accomplished in 410, 614, and 462 s for only L-SEMS, only the N-SEM, and simultaneous use, respectively. The global search algorithm does not always run local solvers at the trial points. The trial points can be rejected according to basin, score, and constraint filters. Therefore, the numbers of local solver calls are 67, 60, and 57 for only L-SEMS, only the N-SEM, and simultaneous use, respectively. Furthermore, the first local solution at the initial guess resulted in the best score among all trial points for only the L-SEM case. Therefore, other trial points could not improve the results, although most of the optimization times are dedicated to generation and analyses of the trial points. For only N-SEMs, the best score is found among the first 200 trial points, and it resulted in an insignificant decrease of 1.5% of the local minimization at the initial guess. However, the solution for simultaneous use is improved several-fold in the first 671 trial points, and the cost function value of the local minimizer at the initial guess decreased to 99.7% at the end of the optimization.

Figure 7 shows the advantage of simultaneously using L-SEMs and the N-SEM with the resulting u-x-y distributions for the same data as in Figure 6. In Equation 5, $u(\mathbf{r})$ is considered as $x^2 + y^2$. The inverse of the $B_1(x, y)$ distribution is called the target correction profile, and it is used to obtain the homogenous excitation profile after the correction. In the u-x-y volume approach, the target profile is mapped onto $\delta(u - x^2 - y^2)$, and

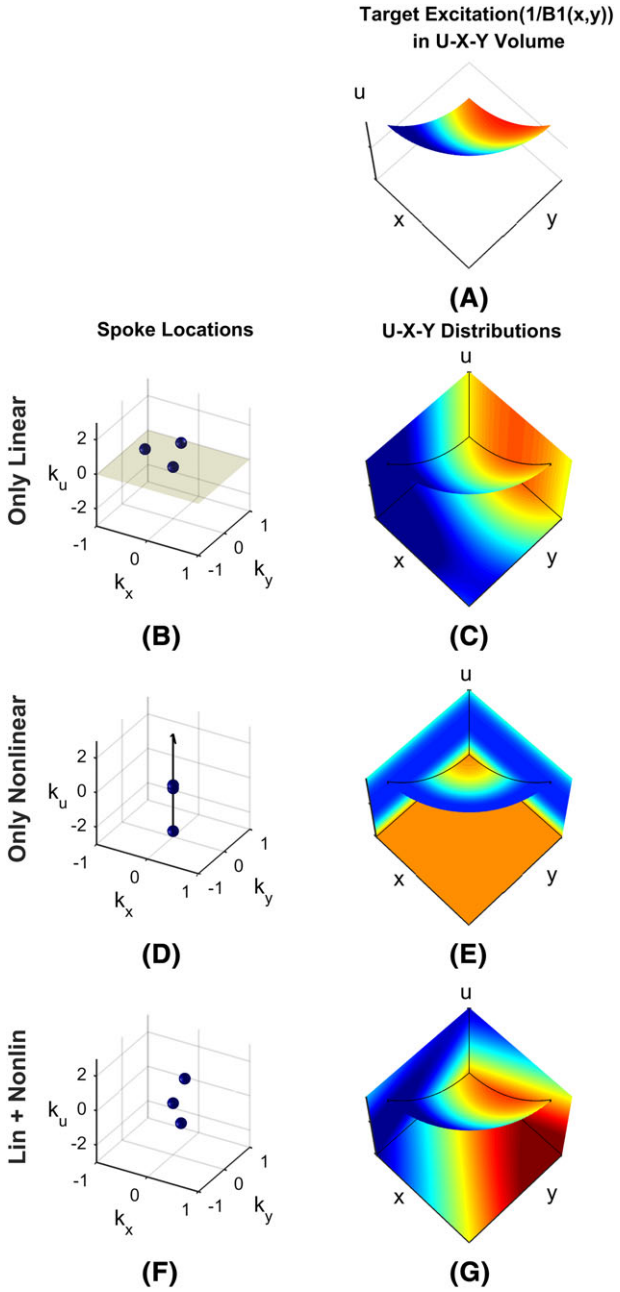

FIGURE 7 Pulse design results for 2D simulations. Spoke locations show the optimized spoke locations for three cases. *u*-*x*-*y* volume distributions show the realized corrections and fourier transform of the spokes. Distributions on $\delta(u - x^2 - y^2)$ are shown, which correspond to actual physical correction of the excitation profile. All *u*-*x*-*y* volume distributions are shown in the first quadrant for simpler visualization. A, The inverse of the $B_1(x, y)$ distribution in Figure 6A is mapped onto $\delta(u - x^2 - y^2)$. B, Optimized spoke locations are on the $k_u = 0$ plane using only L-SEMs. C, In the *u*-*x*-*y* volume, no variation in the *u*-direction is observed. D, Optimized spoke locations are on the $(k_x, k_y) = (0, 0)$ line using only the N-SEM. E, In the *u*-*x*-*y* volume, no variation in the *x*- or *y*-direction is observed. F, Optimized spoke locations are in 3D space using both L-SEMs and the N-SEM. G, In the *u*-*x*-*y* volume, there are variations in all directions

only the first quadrant is shown in Figure 7A. In Figure 7A, only the values on $\delta(u - x^2 - y^2)$ are the design criterion, and the entire volume except for $\delta(u - x^2 - y^2)$ can be filled freely without affecting the excitation. However, the excitation *k*-space can be completely different depending on how the free space is filled. In Figure 7B, spoke locations are restricted to the k_x-k_y plane for only L-SEMs. Figure 7C shows the resulting *u*-*x*-*y* volume distribution, which is also the Fourier transform of the excitation *k*-space in three dimensions. Only the values on the paraboloid correspond to the actual excitation. However, there is no variation in the *u*-direction due to the restriction of spokes to the k_x-k_y plane, which limits the flexibility of the excitation. In Figure 7D, optimized spoke locations are on the k_u line for the correction with only the N-SEM. In Figure 7E, there is no variation in the *x*- or *y*-direction, which limits the correction to being equal at each circle. In Figure 7F, spokes are located in the entire 3D volume, defined by k_x-k_y-k_u, using the L-SEMs and N-SEM together. Therefore, in the corresponding *u*-*x*-*y* volume distribution, variations in all directions are visible, as in Figure 7G, and the actual correction on the paraboloid is a better approximation to the target correction in Figure 7A.

4.3 | Experiments

In the experiments, the spatial dependency of the custom nonlinear gradient coil and the B_0 and B_1 maps at the slice location are required as input for the optimization solver. Corresponding distributions are provided in Figure 8.

Optimization results are presented in Figure 9. The normalized B_1^+ map has a standard deviation of 0.148. If the expected normalized flip angle distributions in the first row of Figure 9 are considered, the standard deviations decrease to 0.119, 0.142, and 0.095 for only L-SEMs, only N-SEMs, and simultaneous use, respectively. In the second row of Figure 9, normalized measured flip angle maps are provided. The standard deviations for the measured flip angle maps are 0.143, 0.158, and 0.121 for only linear, only nonlinear, and simultaneous use. In Figure 9I, simultaneous use of L-SEMs and N-SEM yields a much narrower distribution centered on 1, which is an indication of more uniform excitation.

In the experiment, although the profiles of the expected and measured normalized flip angle maps are similar, for a practical reason that will be explained later, expected and measured normalized flip angle maps have slightly different standard deviations. The root mean square error (RMSE) between the expected and measured flip angle maps is 0.09 for all three cases. The standard deviations are decreased by 20%, 4%, and 46% for only the N-SEM, only L-SEMs, and simultaneous use, respectively. The profiles of the corrected map using only the N-SEM are very similar to the B_1^+ profile, and the very small decrease in the standard deviation suggests that the N-SEM alone is inadequate to correct inhomogeneity. L-

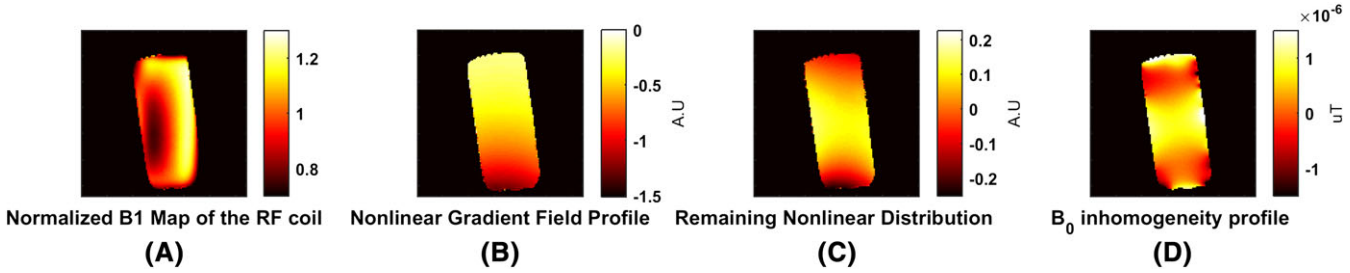

FIGURE 8 Input distributions for optimization. A, Normalized B_1^+ map of the single-channel transmit coil such that the average of B_1^+ over the ROI is 1. B, Spatial dependency of the nonlinear gradient coil over the ROI given in arbitrary units (A.U.). C, Spatially nonlinear distribution of the coil after subtraction of a spatially constant term and LSEM terms from the actual profile of the NSEM coil. D, Deviation of the static magnetic field from the magnetic field corresponding to the adjusted frequency

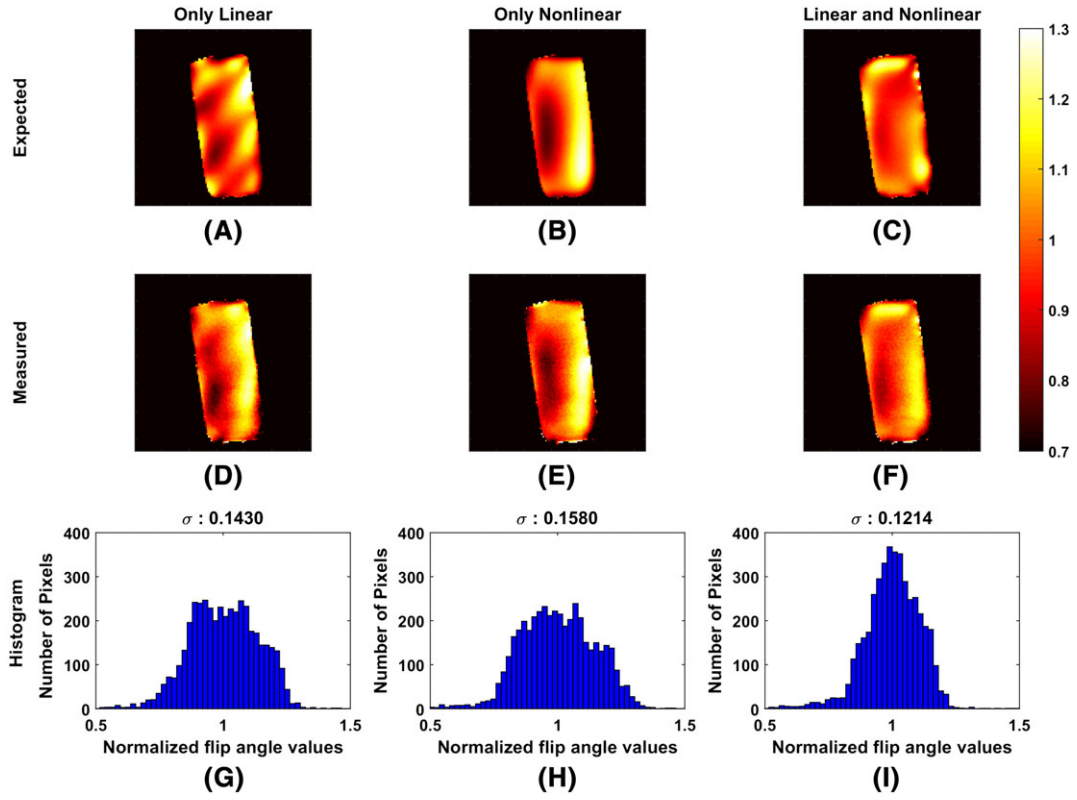

FIGURE 9 Normalized flip angle maps after correction using only L-SEMs, only the N-SEM, and the combination of L-SEMs and the N-SEM. A-C, Normalized expected flip angle distributions after the optimizations for only L-SEMs, only the N-SEM, and simultaneous use of both. D-F, Normalized flip angle distributions measured with the double-angle method for each case. G-I, Histogram of the pixels in the normalized measured flip angle distribution over the ROI. The standard deviation from the average is provided for each case

SEMs alone performed better than the N-SEM alone; however, they provide almost half of the correction provided by simultaneous use. In Figure 9 C,F, the final excitation profiles have almost ideal uniformity except the regions close to edges. One possible reason might be that the algorithm suffers from higher B_0 inhomogeneity at the edges.

5 | DISCUSSION AND CONCLUSIONS

5.1 | Freedom of the simultaneous use of L-SEMs and N-SEMs

Although the simultaneous use of L-SEMs and N-SEMs is harder to interpret and requires more complicated design strategies, driving them with independent time waveforms is the most flexible design for a given target transverse magnetization. For a design framework and better intuition, the excitation *k*-space is formulated in Equation 5 with an increase from three dimensions to four through the inclusion of the N-SEM. According to this formulation, infinitely many different excitation *k*-spaces can lead to the same excitation profile in space. This is demonstrated in Figure 2 with four different examples, resulting in a rectangular 1D excitation profile originating from completely different excitation *k*-spaces that differ in total energy, dimensionality, and length of the required trajectory. A dual approach would be for the *u*-*x* plane to be freely filled (except for the points lying on$\delta\ (u(\boldsymbol{r})-u)$) while altering the excitation *k*-space. However, in Figures 2F,G and 5B,C, the use of only L-SEMs or only the N-SEM leads to only 1D variation in the *u*-*x* plane, which results in suboptimal solutions. As a result of this flexibility, simultaneous use leads to more homogenous excitation profiles than the use of only L-SEMs or only N-SEMs, as in Figures 5, 6, and 9 and Table 1. Especially for the same RF power limit, simultaneous use still performs better than using only L-SEMs. Without this result, one might suspect that homogeneity improvement might be obtained at the expense of increased SAR when L-SEMs and N-SEMs are simultaneously used. However, it is shown that the better performance of simultaneous use is due not to an increase in the SAR but to an increase in the number of degrees of freedom. Because the simultaneous use of L-SEMs and the N-SEM is the generalized case of using only L-SEMs or N-SEMs, improvement in the performance is enabled at the expense of hardware and design complexity.

Although the experimentally measured and simulated flip angle profiles are in agreement, the measured standard deviations of the flip angles are slightly higher than the simulated ones in Figure 9. However, the RMSEs between the measured and simulated flip angle maps are 9% for all cases, which still allows fair comparison between them. There are two main reasons for this in addition to experimental imperfections. First, the double-angle method assumes a linear relationship between the transmit field and flip angle. This linear relation starts to break down after the small tip angle regime, which is 30° for spatially selective excitation pulses.[1] However, small tip angle pulses still work reasonably well up to 90° pulses,[1] and deviations from the linear relation in the double-angle method can be neglected up to 140°.[18] Therefore, the error of the double-angle method in spoke excitation is neglected. Another possible reason for the higher standard deviation in the experiments is that noise is present during the experiments, and nonlinear computation of the double-angle method amplifies the noise.[19] However, simultaneous use also provides better homogeneity in the measured flip angle maps.

In contrast to orthogonal L-SEMs, N-SEMs can be written as a summation of a spatially constant term, L-SEMs, and a remaining spatially nonlinear term, which is very similar to the terminology in Reference [10]. In the spoke excitation with simultaneous use of L-SEMs and N-SEM, a spatially constant term causes a spatially constant phase term for the magnetization that can be provided with the phase of the RF pulse. L-SEM terms in the N-SEM profile can already be provided by the actual L-SEM coils. The remaining spatially nonlinear term is the actual cause of the increase in the number of degrees of freedom. For our example N-SEM coil, the remaining spatially nonlinear term is shown in Figure 8C.

In this work, different example B_1^+ distributions for each case are used. In the case of a general B_1^+, all possible B_1^+ inhomogeneities can be corrected with only L-SEMs theoretically if there is no strict limit on the spoke number. In such a scenario, the freedom resulting from the addition of an N-SEM channel might be used to decrease the RF power or pulse duration. If there is a limit on the spoke number, the remaining spatially nonlinear distribution of the N-SEM channel has a significant impact on the final flip angle homogeneity performance. The increase in the performance is more explicit when the spatial harmonics of the inverse B_1^+ profile can be expressed as a superposition of different combinations of L-SEM and N-SEM profiles. For example, flip angle inhomogeneity is decreased to 96% of the uncorrected case in Figure 5 because the inverse of the B_1 profile has mostly second and first order variations that can be corrected with the simultaneous use of L-SEM (x) and N-SEM (x^2). However, the increase in the performance can vary for different B_1^+ inhomogeneity profiles. For instance, the increase in the performance on adding an additional N-SEM channel is higher for 2D simulations than for experiments because the simulated B_1^+ profile can be better expressed with the available channels in Figure 6. In experiments, the B_1^+ inhomogeneity profile has more variation along the *x*-direction compared to the *z*-direction in Figure 8A, and the remaining spatially nonlinear term has more variation along *z* and less variation along the *x*-direction, as in Figure 8C. However, simultaneous use of L-SEMs and N-SEM could increase the performance in all cases.

Furthermore, static field heterogeneity is not formulated in the excitation *k*-space formulation because it is always present during the RF pulse and cannot be controlled. There are two main drawbacks to B_0 inhomogeneity in spoke excitation. First, if spokes are in the reverse direction, the effects of B_0 inhomogeneity for even and odd spokes are different, which can disturb the expected spoke excitation profile. Therefore, the flyback trajectory is used to avoid this effect, as in Figure 4. In the flyback trajectory, even if the slice profiles are disturbed, they are in phase for all spokes; therefore, the expected spoke excitation can be obtained. To decrease this effect, N-SEM coils can be used as shim coils during the RF pulses if the

N-SEM profile can correct some portion of the B_0 inhomogeneity. The second effect is the probably unwanted phase accumulation due to B_0 inhomogeneity between the RF pulses, and it is already included in the optimization in Equation 6 for correction as far as possible by the N-SEM profile.

5.2 | Comments on related works

In a conference abstract,[20] Grissom et al showed that for a specific transmit array B_1^+ profile the simultaneous use of L-SEMs and N-SEMs in combination with parallel transmission can result in better uniformity, which can be exchanged for a lower number of spokes or a lower number of transmit channels. As an extension to the work of Grissom et al, our study provides a theoretical perspective for understanding the increase in the number of degrees of freedom when additional N-SEMs are included, which is the first experimental validation of the concept with spoke numbers higher than two and considerations of RF power limitations and static field heterogeneity.

Kopanoglu et al have also introduced the excitation *k*-space variables for N-SEMs.[12] These authors used a coordinate transformation from linear spatial variables to nonlinear spatial variables by assuming that encoding fields are bijective, which is generally not the case for higher order spherical harmonics. In their work, the coordinate transformation does not consider the simultaneous use of L-SEMs together with N-SEMs. Furthermore, in Reference [10], the general phase term during the excitation is expressed as a summation of the static nonlinear terms, the dynamic nonlinear terms, and the terms that can be interpreted as commonly known excitation *k*-space variables for L-SEMs. Similarly, Haas et al have used parallel transmission together with only N-SEMs and expressed the total phase term as a summation of independent gradient channels that can have independent time evolutions or space dependencies.[11] Both studies[10,11] have used the direct phase evolution approach in the RF pulse design.

Other works aiming to conduct B_1^+ correction via N-SEMs have used two-spoke excitation with a specific combination of N-SEMs and L-SEMs.[21,22] In References [21,22], the best spatial phase profile that can be generated between the two spokes is analytically derived by assuming the same amplitude and phase for each spoke. The analytical expression is advantageous in terms of computation time, but the fixed number of spokes with the same amplitude and phase can limit the performance of the B_1^+ correction. Later, the required phase profiles were estimated by using L-SEMs and N-SEMs with either second-order static shim coils[21] or 48-channel dynamic MC hardware.[22] Another study[13] has proposed creating the spatial profile as a superposition of the first- and second-order gradients, which should be similar to the inverse profile of B_1^+, to correct B_1^+ inhomogeneity in simulations. In such a scenario, the single excitation *k*-space variable for the superposition of the first- and second-order gradients is defined. Furthermore, it is assumed that the desired target magnetization profile can be parameterized by the gradient encoding fields, which leads to a Fourier transformation relation in a lower dimension between single-excitation *k*-space and transverse magnetization. As an extension of this work, our excitation *k*-space formulation defines independent variables for each N-SEM channel, and a Fourier transform relationship is still re-established in the increased dimension without requiring the parameterization of the target distribution. Later, this work was extended to parallel transmission with a similar design principle for a spatial phase profile.[23] Although the number of spokes is greater than 2, the approach is also suboptimal since it uses the same combination of N-SEMs and L-SEMs for all spokes; in other words, the phase profiles created between the spokes are only linearly scaled versions of each other. Previous methods[13,21-23] might be extremely effective for correcting even highly variant B_1^+ inhomogeneities in space if there is a high number of independent N-SEM channels to implement the required phase profile at the expense of hardware complexity. However, the approaches are still suboptimal because the required phase profile might not be created by the available hardware; therefore, an optimization that considers the available field profiles at the first stage can still be useful.

Although the use of the L-SEMs alone significantly simplifies the theory of MRI, the N-SEMs are already shown to provide additional degrees of freedom to improve the efficiency of both the reception and excitation phases of an imaging sequence. In the reception phase of a pulse sequence, the N-SEMs are utilized in accelerating the scan,[24-27] reducing the FOV,[28] reducing the peripheral nerve stimulation (PNS), and increasing the resolution at the periphery of the object.[29-31] For the excitation part of a pulse sequence, it has been shown that the N-SEMs can be used to excite curved slices,[32-34] reduce the FOV with localized excitation,[16,35-37] and reduce the SAR,[12] in addition to the B_1^+ inhomogeneity correction. Additionally, the dynamic shimming methods using time-varying higher-order spatial field terms[38-41] can be considered as an application for the N-SEMs. Therefore, the clinical applications of MRI can greatly benefit from the N-SEMs in the future, although the design and development of the N-SEM hardware with precise control are still challenging problems.

5.3 | Pulse design

Although the addition of a single-channel N-SEM coil improves the flip angle uniformity, the pulse design problem becomes computationally more expensive due to spoke placement in higher dimensions and an increased number of local minima resulting from the possibility of infinitely many trajectories for the same excitation pattern. The best solution for L-SEMs and N-SEMs would have been obtained if fewer trial points were specified as a stopping criterion. However, the value of the objective function for simultaneous use is still less than that for the use of only L-SEMs or N-SEMs for the first 200 trial points. Therefore, increases in the number of local minima and the number of variables lead to a more complex optimization procedure for simultaneous use of L-SEMs and the N-SEM; however, simultaneous use might still have superior performance in terms of local solutions in comparison with using only L-SEMs or the N-SEM.

Global optimization can also be used to minimize the cost function under the linear or nonlinear inequality constraints, such as maximum distance in the excitation *k*-space, maximum RF average power, or peak power. Furthermore, computation is parallelized, and the computation time

can be limited as applied in the optimizations in the experiments. However, finding the global optimum for a much higher number of N-SEM channels is still a challenging problem, although the scatter search algorithm can find global solutions to the problem of over 100 variables and 100 constraints in one or two local solver calls for most of the nonlinear programming applications.[14] In a practical case with a time limitation, some algorithms for finding the local solutions instead of the global solution can result in a better performance. However, the built-in "GlobalSearch" function in MATLAB is used to demonstrate that the global solution of the simultaneous use of L-SEMs and the N-SEMs can provide more homogeneous excitations than the use of only L-SEMs or N-SEMs.

The pulse design techniques in the literature, which use only L-SEMs, can be utilized to accelerate the computation time or to obtain a better solution in a limited time, although they are not studied for N-SEMs. For instance, it can be shown that the analytical minimum to obtain the most homogenous flip angle distribution for given spoke locations in local gradient-based algorithms[42] is still applicable when L-SEMs and N-SEMs are simultaneously used. A sparsity enforced method can also be adapted to the simultaneous use of L-SEMs and N-SEMs to decrease the spoke numbers.[9] However, the gradient based methods and the sparsity enforced methods do not consider the B_0 effect at the beginning and require retuning after the spoke placement. They can be used for a given target excitation phase distribution, which makes them suboptimal for optimizing only the amplitude distribution. Grissom et al [43] propose an interleaved greedy and local optimization method including target phase optimization. Although their pulse design technique is closer to the global optimum than the abovementioned two methods for the amplitude excitation profile optimization at the expense of computation time, sequential placement of spokes avoids the global optimality. In the "GlobalSearch" optimization, the target excitation phase is not fixed, and the spokes are not placed sequentially for global optimality with a fixed number of spokes. Last, the pulse design process can be extremely accelerated and better homogeneity performance can be managed with fewer spokes if there are numerous channels for obtaining the optimal phase distribution between two spokes at the expense of hardware complexity.[21,22]

Another important consideration for the RF pulse design is the 3D spatial dependency of the N-SEM channel. Due to the zero Laplacian property of static magnetic fields, nonlinear deviation in one direction is likely to cause nonlinear deviation in another direction. Therefore, the field profile of N-SEM channels has through-plane deviations. Under the thin slice approximation, this dependency can be approximated as 2D, and Equation 6 can be valid. If the thin slice approximation fails, two related drawbacks might occur. First, the transverse excitation profile may be changed because through-slice phase accumulation is not uniform in the transverse plane. Second, if there is still through-slice phase dependency after the excitation, signal dephasing inside the pixel will decrease the image intensity. Even if the B_1^+ inhomogeneity is 2D, 3D considerations should be included to correct B_1^+ inhomogeneity in thicker slices or slabs with N-SEMs. In the prototype coil, simulations suggest that the field profile can deviate from 1% to 2% in the slice direction for each pixel. For the field measurement, one reference GRE image and another GRE image with a blip current applied to the N-SEM channel are obtained. Due to signal dephasing not only in the slice direction but also in all 3D pixel volumes, the average amplitude was 3% lower in the GRE image with blip current. During field measurements the maximum phase deviation was lower than π, and during the spoke excitation the most distant spoke location was −0.65, as in Table 1, which suggests that 2% in-slice phase deviation of the total 0.65π phase is present during the excitation in a worst-case scenario. Such a phase distribution is negligible in our case, which is consistent with the match between measured and expected flip angle maps in Figure 9; however, the in-slice dependency of N-SEM channels must be carefully considered in other applications.

5.4 | Practical considerations

The design of a human-size N-SEM gradient coil should consider many practical issues such as inductance, DC and AC resistance, force, torque, available physical space in the scanner, heat exchange, mechanical design, patient comfort, and shielding. Furthermore, an N-SEM coil should be able to create enough field variation and slew rate considering the current and voltage limitations of the amplifier, respectively, and the power requirements of the gradient amplifiers are proportional to the fifth power of the coil dimensions.[44] Although coil and amplifier design is beyond the scope of this paper, a prototype N-SEM coil is manufactured as proof of concept with a diameter of 20 cm to fit inside the scanner, and it is torque balanced due to angular symmetry. However, the pulse design techniques and theoretical formulations would have been valid if a human-size N-SEM coil had been available. The switching times of N-SEM coils must be further investigated when they are simultaneously used with L-SEMs in a human experiment. From the hardware perspective, switching times are mostly determined by the voltage of the amplifier; however, physiological factors, such as PNS, generally determine the limits. Depending on the vector E-field distributions of the N-SEMs and L-SEMs, new PNS limitations should be determined considering the superposition of the fields during simultaneous use. In spoke excitation, the optimal phase distribution is generally smooth between the RF pulses to correct slowly varying transmit heterogeneity. The dead space between the RF pulses due to the rise and fall times of the slice select gradient is generally enough to switch the required small current values of N-SEM coils. Even if the dead space is insufficient, the excitation k-space is designed in this work, and realizing a specific excitation k-space with RF and gradient waveforms can be solved by including slew rate considerations. However, the VERSE excitation[45] or receive purposes are generally more demanding in terms of slew rate, and the simultaneous use of N-SEMs and L-SEMs requires further investigation.

Because the custom coil system does not have a shield, the eddy current and the coupling issues are also considered. Coupling from our coil to system gradients is neglected since the shield of the system gradients almost cancels the net effect. More importantly, the coupling from system gradients to the custom coil is stronger. When the custom coil is placed at the isocenter of the scanner, the x- and y-gradients do not cause any coupling problems since the net flux passing through the custom coil is 0; however, such symmetry does not exist for the z-gradient. Thus, the slew rate is minimized for all system gradient waveforms. The eddy current effects are considered in two classes: short and long time constant eddy

currents. For the short time constant eddy currents, most of the effect exists in the same duration as the current applied to the custom coil. In the measurement of the field profile on the slice of interest and spoke sequences, a triangular current waveform that is exactly the same except for the amplitude is used. Therefore, fast decaying eddy current effects are considered in the field profile and should be the same for the spoke sequence assuming that the eddy current effects are linear. As mentioned in previous works,[46] for long lasting eddy current effects, if the duration of the current waveform is very small compared with the time constant, the eddy currents caused by rising and falling edges tend to cancel each other out. Therefore, a very fast triangular current waveform is used to drive the custom coil. As a result, eddy current and coupling effects for the custom coil are mostly counteracted.

5.5 | Possible enhancements

In this study, defining an independent excitation *k*-space for N-SEMs is shown to provide freedom and improvements in correcting the B_1^+ inhomogeneity. Very similar techniques can be used for FOV reduction and slice selection. Additionally, the excitation *k*-space can be designed in such a way that shorter trajectories or lower SAR RF pulses can lead to the same excitation profiles. Furthermore, although spoke excitation is used in this study, in principle, time-varying gradient waveforms can be played during the RF pulse to traverse curved *k*-space trajectories and allow more freedom to optimize the solution.

The independent excitation *k*-space formulation trivially allows for increasing the number of N-SEMs. Although computationally more expensive, it might provide a dramatic improvement in the performance. Instead of using multiple N-SEMs, it is shown that the addition of each N-SEM increases the dimension of the degrees of freedom in the RF excitation problem. Existing gradient coil arrays in References [21,22,29,40] and dynamic second-order coils can be utilized under the proposed technique. Furthermore, alternative linear gradient coil designs[47-49] can be used to generate nonlinear gradients, although they have been designed for flexible linear gradient systems. Further, parallel excitation techniques[5,6] can be combined with the proposed method if the formulation is generalized. Last, although this study only considers the small tip angle excitation regime, the formulation might be extended in a similar manner to large tip angle pulses since the excitation *k*-space concept is still present for Cayley-Klein parameters in the small excitation solution of large tip angle pulses.[50]

ACKNOWLEDGEMENTS

The authors thank Taner Demir, Umut Gundogdu, and Soheil Taraghinia for their participation in valuable discussions regarding the experimental setup and Yıldıray Gökhalk for the production of the custom-made nonlinear gradient coil. Sponsors: Grant 1001-112E555 from TUBITAK (The Scientific and Technological Research Council of Turkey).

REFERENCES

1. Pauly J, Nishimura D, Macovski A. A k-space analysis of small-tip-angle excitation. *J Magn Reson*. 1989;81:43-56.
2. Vaughan JT, Garwood M, Collins C, et al. 7T vs. 4T: RF power, homogeneity, and signal-to-noise comparison in head images. *Magn Reson Med*. 2001;46:24-30.
3. de Moortele V, Akgun C, Adriany G, et al. B_1 destructive interferences and spatial phase patterns at 7 T with a head transceiver array coil. *Magn Reson Med*. 2005;54:1503-1518.
4. Mao W, Smith MB, Collins CM. Exploring the limits of RF shimming for high-field MRI of the human head. *Magn Reson Med*. 2006;56:918-922.
5. Katscher U, Bornert P, Leussler C, van den Brink JS. Transmit SENSE. *Magn Reson Med*. 2003;49:144-150.
6. Collins CM, Liu W, Swift BJ, Smith MB. Combination of optimized transmit arrays and some receive array reconstruction methods can yield homogeneous images at very high frequencies. *Magn Reson Med*. 2005;54:1327-1332.
7. Saekho S, Yip CY, Noll DC, Boada FE, Stenger VA. Fast-k_z three-dimensional tailored radiofrequency pulse for reduced B_1 inhomogeneity. *Magn Reson Med*. 2006;55:719-724.
8. Zelinski AC, Wald LL, Setsompop K, et al. Fast slice-selective radio-frequency excitation pulses for mitigating B_1^+ inhomogeneity in the human brain at 7 Tesla. *Magn Reson Med*. 2008;59:1355-1364.
9. Zelinski AC, Wald LL, Setsompop K, Goyal VK, Adalsteinsson E. Sparsity-enforced slice-selective MRI RF excitation pulse design. *IEEE Trans Med Imaging*. 2008;27:1213-1229.
10. Schneider JT, Haas M, Ruhm W, Hennig J, Ullmann P. Robust spatially selective excitation using radiofrequency pulses adapted to the effective spatially encoding magnetic fields. *Magn Reson Med*. 2011;65:409-421.
11. Haas M, Ullmann P, Schneider J, et al. PexLoc—Parallel excitation using local encoding magnetic fields with nonlinear and nonbijective spatial profiles. *Magn Reson Med*. 2013;70:1220-1228.
12. Kopanoglu E, Yilmaz U, Gokhalk Y, Atalar E. Specific absorption rate reduction using nonlinear gradient fields. *Magn Reson Med*. 2013;70:537-546.
13. Hsu YC, Chern IL, Zhao W, Gagoski B, Witzel T, Lin FH. Mitigate B_1^+ inhomogeneity using spatially selective radiofrequency excitation with generalized spatial encoding magnetic fields. *Magn Reson Med*. 2014;71:1458-1469.
14. Ugray Z, Lasdon L, Plummer J, Glover F, Kelly J, Martí R. Scatter search and local NLP solvers: A multistart framework for global optimization. *INFORMS J Comput*. 2007;19:328-340.
15. Sacolick LI, Wiesinger F, Hancu I, Vogel MW. B1 mapping by Bloch-Siegert shift. *Magn Reson Med*. 2010;63:1315-1322.
16. Kopanoglu E, Constable RT. Radiofrequency pulse design using nonlinear gradient magnetic fields. *Magn Reson Med*. 2015;74:826-839.
17. Childs AS, Malik SJ, O'Regan DP, Hajnal JV. Impact of number of channels on RF shimming at 3T. *Magn Reson Mater Phys Biol Med*. 2013;26:401-410.

18. Stollberger R, Wach P. Imaging of the active B_1 field *in vivo*. *Magn Reson Med*. 1996;35:246-251.
19. Cunningham CH, Pauly JM, Nayak KS. Saturated double-angle method for rapid B_1^+ mapping. *Magn Reson Med*. 2006;55:1326-1333.
20. Grissom W, Sacolick L, Vogel M. B_1+ inhomogeneity compensation using 3D parallel excitation is enhanced by simultaneous linear and nonlinear gradient encoding. *Proc Int Soc Magn Reson Med*. 2011;19:2898
21. Duan Q, van Gelderen P, Duyn J. Tailored excitation using nonlinear B_0-shims. *Magn Reson Med*. 2012;67:601-608.
22. Umesh Rudrapatna S, Juchem C, Nixon TW, de Graaf RA. Dynamic multi-coil tailored excitation for transmit B_1 correction at 7 Tesla. *Magn Reson Med*. 2015; https://doi.org/10.1002/mrm.25856
23. Hsu YC, Lattanzi R, Chu YH, Cloos MA, Sodickson DK, Lin FH. Mitigation of B_1^+ inhomogeneity using spatially selective excitation with jointly designed quadratic spatial encoding magnetic fields and RF shimming. *Magn Reson Med*. 2016; https://doi.org/10.1002/mrm.26397
24. Stockmann JP, Ciris PA, Galiana G, Tam L, Constable RT. *O*-space imaging: Highly efficient parallel imaging using second-order nonlinear fields as encoding gradients with no phase encoding. *Magn Reson Med*. 2010;64:447-456.
25. Tam LK, Stockmann JP, Galiana G, Constable RT. Null space imaging: Nonlinear magnetic encoding fields designed complementary to receiver coil sensitivities for improved acceleration in parallel imaging. *Magn Reson Med*. 2012;68:1166-1175.
26. Weber H, Schultz G, Gallichan D, Hennig J, Zaitsev M. Local field of view imaging for alias-free undersampling with nonlinear spatial encoding magnetic fields. *Magn Reson Med*. 2014;71:1002-1014.
27. Layton KJ, Gallichan D, Testud F, et al. Single shot trajectory design for region-specific imaging using linear and nonlinear magnetic encoding fields. *Magn Reson Med*. 2013;70:684-696.
28. Wiesler DG, Wen H, Wolff SD, Balaban RS. Reduction of field of view in MRI using a surface-spoiling local gradient insert. *J Magn Reson Imaging*. 1998;8:981-988.
29. Hennig J, Welz AM, Schultz G, et al. Parallel imaging in non-bijective, curvilinear magnetic field gradients: A concept study. *Magn Reson Mater Phys Biol Med*. 2008;21:5-14.
30. Gallichan D, Cocosco CA, Dewdney A, et al. Simultaneously driven linear and nonlinear spatial encoding fields in MRI. *Magn Reson Med*. 2011;65:702-714.
31. Schultz G, Ullmann P, Lehr H, Welz AM, Hennig J, Zaitsev M. Reconstruction of MRI data encoded with arbitrarily shaped, curvilinear, nonbijective magnetic fields. *Magn Reson Med*. 2010;64:1390-1403.
32. Börnert P, Schäffter T. Curved slice imaging. *Magn Reson Med*. 1996;36:932-939.
33. Weber H, Gallichan D, Schultz G, et al. Excitation and geometrically matched local encoding of curved slices. *Magn Reson Med*. 2013;69:1317-1325.
34. Weber H, Haas M, Kokorin D, Gallichan D, Hennig J, Zaitsev M. Local shape adaptation for curved slice selection. *Magn Reson Med*. 2014;72:112-123.
35. Ma C, Xu D, King KF, Liang ZP. Reduced field-of-view excitation using second-order gradients and spatial-spectral radiofrequency pulses. *Magn Reson Med*. 2013;69:503-508.
36. Witschey WR, Cocosco CA, Gallichan D, et al. Localization by nonlinear phase preparation and *k*-space trajectory design. *Magn Reson Med*. 2012;67:1620-1632.
37. Islam H, Glover GH. Reduced field of view imaging using a static second-order gradient for functional MRI applications. *Magn Reson Med*. 2015; https://doi.org/10.1002/mrm.25650
38. Juchem C, Nixon TW, McIntyre S, Boer VO, Rothman DL, de Graaf RA. Dynamic multi-coil shimming of the human brain at 7 T. *J Magn Reson*. 2011;212:280-288.
39. Juchem C, Umesh Rudrapatna S, Nixon TW, de Graaf RA. Dynamic multi-coil technique (DYNAMITE) shimming for echo-planar imaging of the human brain at 7 Tesla. *Neuroimage*. 2015;105:462-472.
40. Harris C, Handler WB, Chronik BA. A new approach to shimming: The dynamically controlled adaptive current network. *Magn Reson Med*. 2014;71:859-869.
41. Witschey WR, Littin S, Cocosco CA, et al. Stages: Sub-Fourier dynamic shim updating using nonlinear magnetic field phase preparation. *Magn Reson Med*. 2014;71:57-66.
42. Ma C, Xu D, King KF, Liang ZP. Joint design of spoke trajectories and RF pulses for parallel excitation. *Magn Reson Med*. 2011;65:973-985.
43. Grissom WA, Khalighi MM, Sacolick LI, Rutt BK, Vogel MW. Small-tip-angle spokes pulse design using interleaved greedy and local optimization methods. *Magn Reson Med*. 2012;68:1553-1562.
44. Bowtell R, Mansfield P. Gradient coil design using active magnetic screening. *Magn Reson Med*. 1991;17:15-21.
45. Conolly S, Nishimura D, Macovski A, Glover G. Variable-rate selective excitation. *J Magn Reson*. 1988;78:440-458.
46. Alexander AL, Tsuruda JS, Parker DL. Elimination of eddy current artifacts in diffusion-weighted echo-planar images: The use of bipolar gradients. *Magn Reson Med*. 1997;38:1016-1021.
47. Kimmlingen R, Gebhardt M, Schuster J, Brand M, Schmitt F, Haase A. Gradient system providing continuously variable field characteristics. *Magn Reson Med*. 2002;47:800-808.
48. Harvey PR, Katznelson E. Modular gradient coil: A new concept in high-performance whole-body gradient coil design. *Magn Reson Med*. 1999;42:561-570.
49. Parker DL, Hadley JR. Multiple-region gradient arrays for extended field of view, increased performance, and reduced nerve stimulation in magnetic resonance imaging. *Magn Reson Med*. 2006;56:1251-1260.
50. Pauly J, Nishimura D, Macovski A. A linear class of large-tip-angle selective excitation pulses. *J Magn Reson*. n82:571-587.

How to cite this article: Ertan K, Atalar E. Simultaneous use of linear and nonlinear gradients for B_1^+ inhomogeneity correction. *NMR in Biomedicine*. 2017;30:e3742. https://doi.org/10.1002/nbm.3742